# Novel online fitting algorithm for impedance-based state estimation of Li-ion batteries

1st Jussi Sihvo
*Department of Electrical Engineering*
*Tampere University*
Tampere, Finland
jussi.sihvo@tuni.fi

2nd Tomi Roinila
*Department of Electrical Engineering*
*Tampere University*
Tampere, Finland
tomi.roinila@tuni.fi

3rd Tuomas Messo
*Department of Electrical Engineering*
*Tampere University*
Tampere, Finland
tuomas.messo@tuni.fi

4th Daniel-Ioan Stroe
*Department of Energy Technology*
*Aalborg University*
Aalborg, Denmark
dis@et.aau.dk

***Abstract*—The impedance of a Li-ion battery is an important parameter for the battery's state-of-charge (SOC) and state-of-health (SOH) estimation. Battery impedance is typically modeled by an equivalent-circuit-model (ECM) in which the variations in the specific model parameters can be used for estimating the SOC and the SOH. However, the fact that the battery impedance is highly non-linear complicates the parameterization of the model. The model is traditionally obtained by a complex non-linear least-squares fitting algorithm which comes with high complexity. This paper proposes a novel approach to extract all the ECM parameters of the battery impedance obtained with online-capable pseudo-random-sequence (PRS) measurements. Although the algorithm has low complexity, it still captures the desired variations in the ECM parameters as a function of SOC. The algorithm is validated for the impedance data from a lithium-iron-phosphate cell.**

***Index Terms*—Li-ion batteries, PRS, Online impedance measurements, SOC, SOH, State-estimation**

## I. Introduction

Li-ion battery technologies are widely recognized as a state-of-the-art solution for energy storages in electrical transportation and renewable energy source applications [1]. The increasing power and energy levels in these applications will make it necessary to improve the safety and performance of battery storages. Li-ion battery storages are usually equipped with a battery management system that actively monitors the state-of-charge (SOC) and the state-of-health (SOH) indirectly by voltage, current and temperature measurements [2]–[4]. The Coulomb counting method and voltage profile methods have conventionally been used for SOC estimation, while the capacity fade and the internal resistance increase have been utilized in the SOH estimation [2]. However, the temperature has a strong non-linear dependency on the SOC and the SOH that weakens the performance of the methods. Moreover, the unequal capacities and aging of the individual cells in the battery pack complicates the estimation of the SOC and the SOH even more. As the number of the series and parallel connected cells in battery storages increases, the conventional state-estimation methods may not meet the demands of the battery applications in the future.

Because battery impedance has been shown to have a strong dependency on the battery SOC and the SOH, [3], [4], the online measurements of the battery impedance can be utilized for estimating the SOC and the SOH. However, the measurements for online applications should be accurate, fast, and computationally light to implement. A common approach for obtaining the battery impedance is applying non-parametric frequency-response measurement [5]. In the method, the battery output current is perturbed (for example, through battery charger) and the resulting output voltage is measured. Fourier methods are then applied to extract the impedance information. Most often, a sine sweep or multi-sines are applied as a perturbation [6]–[8]. The sine sweep typically provides the impedance with high accuracy, but the method is difficult to implement in practical low-cost applications as the sweep contains a large number of different signal levels. An interesting alternative is to use pseudo-random-sequence (PRS) signals, which are simple to implement and capable for producing fast impedance measurements. Such signals have already been successfully applied in several battery and renewable-energy applications [5], [9]–[13].

In order to study the SOC and SOH dependency and reduce the data of the measured impedance, the impedance data is mapped to the equivalent-circuit-model (ECM) parameters [14]–[18]. However, the battery impedance is often highly non-linear and accurate modeling requires complex ECMs, which complicates the fitting procedure. Algorithms such as complex-non-linear-least-squares (CNLS) method are typically used to fit the impedance data to the model in offline applications [16], [17]. The drawback of the CNLS method is that it requires high computational effort. However, the shape of the measured impedance preserves the information about the ECM parameters [14], [15], [18] although the methods

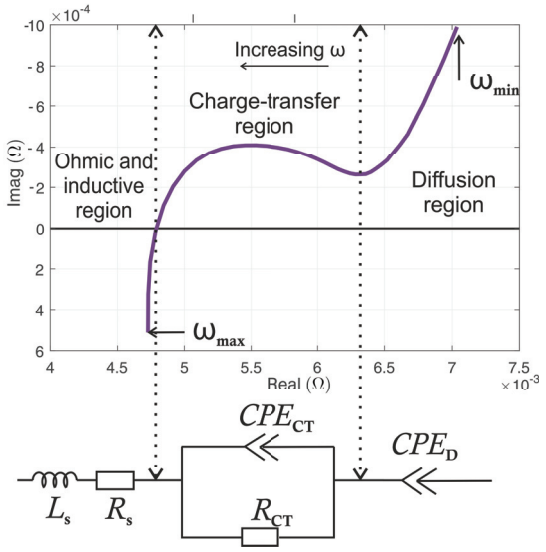


Fig. 1: Impedance plot of a LiFePO4 battery cell and the used ECM of the impedance

for extracting specific parameters for the ECM (such as the suppression factors and capacitors) are yet to be derived accurately. Therefore, a systematic approach to obtain all the ECM parameters makes it possible to fit the ECM parameters to the impedance data with low complexity and good performance.

This work proposes a simple and fast extraction algorithm of the ECM parameters based on the characteristic trends of the measured impedance data. The proposed algorithm is applied for practical impedance measurements from a lithium-iron-phosphate (LiFePo4) cell carried out with the three-level PRS signal [9], [11]. In addition, it is shown that some of the ECM parameters fitted by the proposed method is dependent on the SOC of the battery which proves the method's capability for battery state-estimation.

The rest of the paper is organized as follows. The applied impedance ECM model is presented in Section II and the proposed fitting algorithm is introduced in Section III. The PRS signal used for the impedance measurements is designed and discussed in Section IV. The experiments and the obtained results are discussed and presented in Sections. V and VI, respectively. Conclusions are drawn in Section VII.

## II. Impedance model

The impedance of a LiFePo4-cell with the corresponding ECM are shown in Fig. 1. The impedance can be separated into regions caused by different electrochemical processes inside the battery cell and each region has its counterpart in the applied ECM [7], [16]. The impedance at the charge-transfer and diffusion regions is highly non-linear which is why a non-linear constant-phase-element (CPE) is applied in the ECM. The CPE is expressed mathematically as

$$Z_{\text{CPE}} = \frac{1}{(j\omega)^N C}, \tag{1}$$

where $C$ is the capacitance and $N$ is the suppression factor having values between 0 and 1. Therefore, the impedance of the CPE is realized as a constant slope in the complex plane so the CPE solely models the diffusion region sufficiently. For the charge-transfer region impedance, the parallel connection of a CPE and a resistor can be used to model the suppressed semi-circle shape in Fig. 1. The impedance behavior at the ohmic and inductive region can be modeled with a series resistor and an inductor. The ECM in Fig. 1 can be expressed as

$$Z_{\text{ECM}} = j\omega L_{\text{s}} + R_{\text{s}} + Z_{\text{CT}} + Z_{\text{D}} \tag{2}$$

where $L_{\text{s}}$ is the inductance of the series inductor and $R_{\text{s}}$ is the series resistance. $Z_{\text{CT}}$ represents the charge-transfer region impedance given in (3). For the parametrization of the model, it is convenient to separate the impedance real and imaginary parts of the $Z_{\text{CT}}$ which are given in (4) and (5) respectively. $Z_{\text{D}}$ represents the diffusion region impedance given in (6) both in the complex form and with separated real and imaginary parts.

$$Z_{\text{CT}} = \frac{1}{\frac{1}{R_{\text{CT}}} + (j\omega)^{N_{\text{CT}}} C_{\text{CT}}} \tag{3}$$

$$Z_{\text{CT-re}} = \frac{R_{\text{CT}} + \cos(\frac{\pi N_{\text{CT}}}{2}) R_{\text{CT}}^2 C_{\text{CT}} \omega^{N_{\text{CT}}}}{1 + 2\cos(\frac{\pi N_{\text{CT}}}{2}) R_{\text{CT}} C_{\text{CT}} \omega^{N_{\text{CT}}} + \omega^{2N_{\text{CT}}} R_{\text{CT}}^2 C_{\text{CT}}^2} \tag{4}$$

$$Z_{\text{CT-im}} = \frac{-j\sin(\frac{\pi N_{\text{CT}}}{2}) R_{\text{CT}}^2 C_{\text{CT}} \omega^{N_{\text{CT}}}}{1 + 2\cos(\frac{\pi N_{\text{CT}}}{2}) R_{\text{CT}} C_{\text{CT}} \omega^{N_{\text{CT}}} + \omega^{2N_{\text{CT}}} R_{\text{CT}}^2 C_{\text{CT}}^2} \tag{5}$$

$$Z_{\text{D}} = \frac{1}{(j\omega)^{N_{\text{D}}} C_{\text{D}}} \Longleftrightarrow Z_{\text{D}} = \frac{\cos(\frac{\pi N_{\text{D}}}{2})}{\omega^{N_{\text{D}}} C_{\text{D}}} - \frac{j\sin(\frac{\pi N_{\text{D}}}{2})}{\omega^{N_{\text{D}}} C_{\text{D}}} \tag{6}$$

## III. Proposed fitting algorithm

The diffusion region impedance can be configured separately because its influence at higher frequencies can be considered negligible. The parametrization of $Z_{\text{D}}$ also requires an approximation that the diffusion region is a constant slope, which is the case when neglecting the very low frequencies from the model. In reality, the diffusion region will swerve towards the real axis usually at the frequencies below 100mHz which will make the fitting more difficult [17]. Moreover, the time-consuming nature of measuring very low frequencies is challenging in terms of online applications.

The diffusion region impedance is illustrated in Fig. 2 where $R$ symbols represent the real part of the specific data point and $X$ the corresponding imaginary part. The suppression factor $N_{\text{D}}$ is defined by the angle between the diffusion region impedance and the real axis [15]. Thus, $N_{\text{D}}$ can be obtained as

$$N_{\text{D}} = \frac{2}{\pi}\text{atan}(\frac{X(1) - X(2)}{R(1) - R(2)}) \tag{7}$$

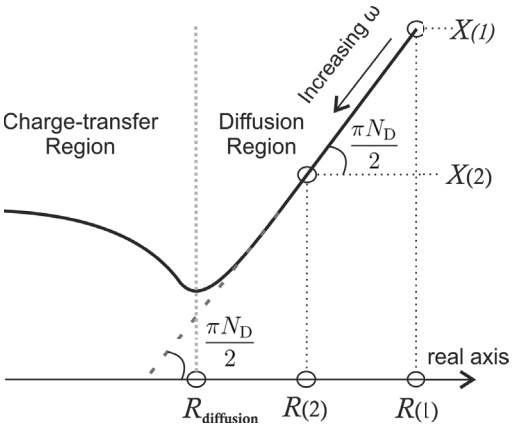


Fig. 2: Parameter illustration of $Z_{\mathrm{D}}$ -element characterizing the diffusion region impedance

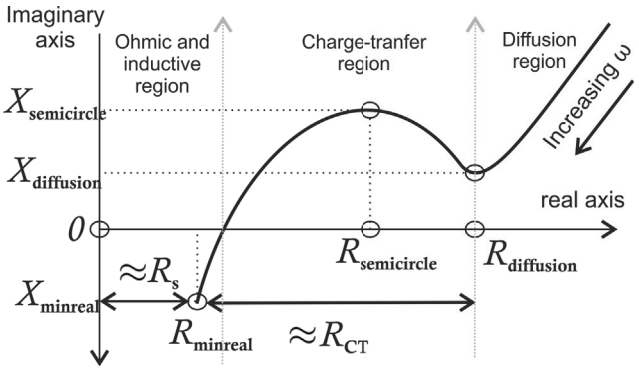


Fig. 3: Parameter illustration of the impedance model parameters in the charge-transfer region and ohmic/inductive region

where $R(1)$ and $R(2)$ are the real parts and $X(1)$ and $X(2)$ are the imaginary parts of the two arbitrary datapoints in the diffusion region. The value for $C_{\mathrm{D}}$ can then be calculated from the imaginary part in (6) as given in (8).

$$C_2 = -\frac{\sin(\frac{\pi N_{\mathrm{D}}}{2})}{\omega_1^{N_{\mathrm{D}}} X(1)} \tag{8}$$

The effect of the parameters to the impedance at the charge-transfer, ohmic and inductive regions are shown in Fig. 3. The derivation starts by obtaining the resistors $R_{\mathrm{diffusion}}$, $R_{\mathrm{semicircle}}$ and $X_{\mathrm{semicircle}}$ from the impedance data. $R_{\mathrm{s}}$, given by the minimum real part of the impedance, is obtained from (9), while $R_{\mathrm{CT}}$ can be derived from (10) [14].

$$R_{\mathrm{s}} \approx R_{\mathrm{minreal}} \tag{9}$$

$$R_{\mathrm{CT}} \approx R_{\mathrm{diffusion}} - R_{\mathrm{s}} \tag{10}$$

The value for $N_{\mathrm{CT}}$ can be derived roughly by using only $Z_{\mathrm{CT}}$ and neglecting the other parts in (2). When obtaining the zero derivative of (5) in terms of $\omega^{N_{\mathrm{CT}}}$ and substituting the resulting $\omega^{N_{\mathrm{CT}}}$ back to (5), the following relation at the top of the semicircle for $Z_{\mathrm{CT}}$ can be obtained.

$$X_{\mathrm{semicircle}} = \frac{R_{\mathrm{CT}} \sin(\frac{\pi N_{\mathrm{CT}}}{2})}{2(\cos(\frac{\pi N_{\mathrm{CT}}}{2}) + 1)} \tag{11}$$

It yields from (11) that $X_{\mathrm{semicircle}}$ is independent of the capacitor value and is defined only by $N_{\mathrm{CT}}$ and $R_{\mathrm{CT}}$. Therefore, $N_{\mathrm{CT}}$ can be solved from (11) with the use of trigonometric identities as given in (12).

$$N_{\mathrm{CT}} = \frac{4}{\pi} \mathrm{atan}(\frac{X_{\mathrm{semicircle}}}{\frac{R_{\mathrm{CT}}}{2}}) \tag{12}$$

Note that (12) is valid for the ideal case where $Z_{\mathrm{CT}}$ solely defines the model impedance without the rest of the parameters in (2). In reality, the inductor will affect the imaginary part value at the top of the semicircle, as well as the previously obtained value for $R_{\mathrm{CT}}$, which will be readjusted in the later parts of the algorithm. Nevertheless, (12) gives a rough estimate for the suppression factor and an accurate fit can be produced even with the applied simplifications, as will be shown later in this paper. The top of the semicircle impedance is also utilized for the extraction of $C_{\mathrm{CT}}$. The real-part of $Z_{\mathrm{CT}}$ in (4) can be arranged in terms of $C_{\mathrm{CT}}$ as in (13), from which the solution for $C_{\mathrm{CT}}$ is given by the quadratic equation. The derivation of $C_{\mathrm{CT}}$ from the real part is useful because inductance $L_{\mathrm{s}}$ is not required for the calculation at this point, as it would be if using the corresponding imaginary part.

$$\begin{aligned} &R_{\mathrm{semicircle}} R_{\mathrm{CT}}^2 \omega_{\mathrm{semicircle}}^{2N_{\mathrm{CT}}} C_{\mathrm{CT}}^2 \\ &+ \cos(\frac{\pi N_{\mathrm{CT}}}{2}) R_{\mathrm{CT}} \omega_{\mathrm{semicircle}}^{N_{\mathrm{CT}}} (2 * R_{\mathrm{semicircle}} - R_{\mathrm{CT}}) C_{\mathrm{CT}} \\ &+ (R_{\mathrm{semicircle}} - R_{\mathrm{CT}}) = 0 \end{aligned} \tag{13}$$

Finally, $L_{\mathrm{s}}$ can be solved from (5) (with the inductor included) at the point where the impedance minimum real part is reached.

$$\begin{aligned} L_{\mathrm{s}} = &\frac{X_{\mathrm{minreal}}}{\omega_{\mathrm{minreal}}} \\ &+ \frac{\sin(\frac{\pi N_{\mathrm{CT}}}{2}) R_{\mathrm{CT}}^2 C_{\mathrm{CT}} \omega_{\mathrm{minreal}}^{N_{\mathrm{CT}}}}{(\omega_{\mathrm{minreal}} + 2\cos(\frac{\pi N_{\mathrm{CT}}}{2}) R_{\mathrm{CT}} C_{\mathrm{CT}} \omega_{\mathrm{minreal}}^{N_{\mathrm{CT}}+1} + \omega_{\mathrm{minreal}}^{2N_{\mathrm{CT}}+1} R_{\mathrm{CT}}^2 C_{\mathrm{CT}}^2)} \end{aligned} \tag{14}$$

The steps applied for the algorithm in (7) - (14) are regarded as the initialization. This is because the resulting fit is not likely to match the measurement data immediately due to the simplifications made to the model during the initialization. In particular, the values for $R_{\mathrm{CT}}$ and $R_{\mathrm{s}}$ should be re-adjusted by substituting the initialized values to (2) and obtaining new real and imaginary part values at the end of the diffusion part and at the top of the semicircle, as well as for the minimum real part from the model. New values for $R_{\mathrm{s}}$ and $R_{\mathrm{CT}}$ are then updated according to (15) and (16), where the single quote denotes the updated value from the model. The values without the single

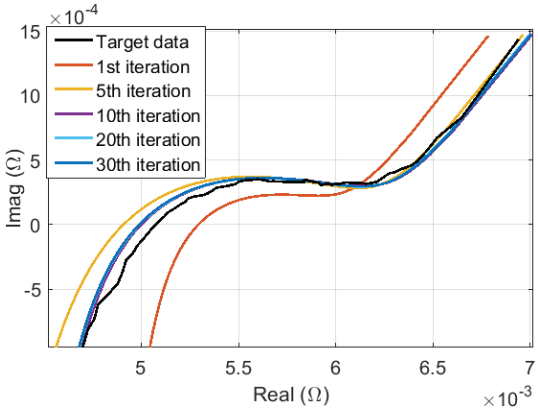


Fig. 4: Illustration of the convergence of the fitting algorithm

quote are the initial values extracted from the measurement data.

$$R_{\mathrm{s}} = R_{\mathrm{s}} + (R'_{\mathrm{minreal}} - R_{\mathrm{minreal}}) \tag{15}$$

$$R_{\mathrm{CT}} = R_{\mathrm{CT}} + (R'_{\mathrm{diffusion}} - R_{\mathrm{diffusion}}) \tag{16}$$

After applying (15) and (16), (13) and (14) will be repeated. Therefore, the algorithm is iterative but will rapidly converge as shown in Fig. 4, where the $10^{\mathrm{th}}$ iteration is already providing good fit. By way of conclusion, the algorithm is step-wisely clarified in Fig. 5.

## IV. Impedance Measurements

The impedance measurements are carried out by injecting the current of the battery cell with a carefully designed perturbation signal, which generates a voltage response according to the battery impedance dynamics. The measured current and voltage can then be Fourier-transformed to obtain the frequency characteristics of the measurements. The impedance

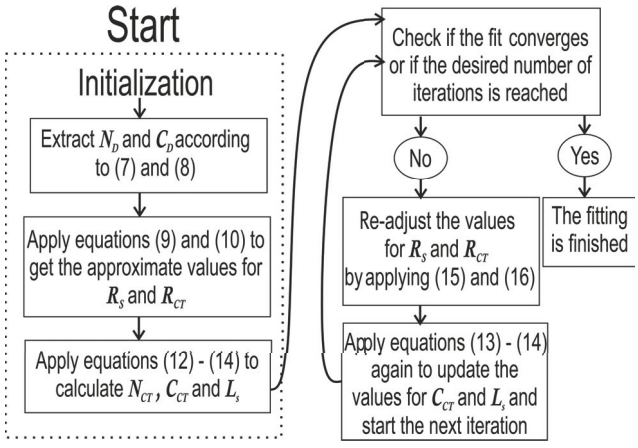


Fig. 5: Step-by-step block diagram of the proposed fitting algorithm

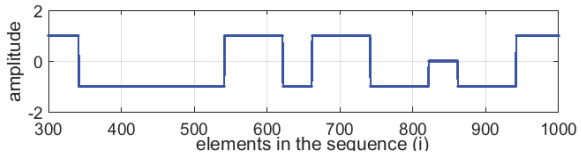


Fig. 6: Time-domain representation of the ternary-sequence perturbation

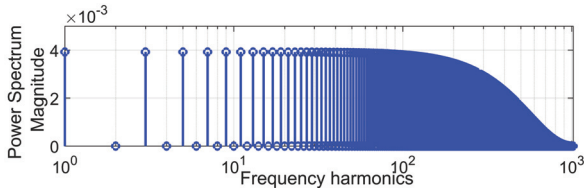


Fig. 7: Frequency-domain representation of the ternary-sequence perturbation

can then be obtained according to the well-known Ohm's law in the frequency domain as

$$Z(j\omega) = \frac{V(j\omega)}{I(j\omega)} \tag{17}$$

For the perturbation signal, a three-level ternary PRS signal is used due to its good performance for measuring non-linear systems [10]–[12]. Besides the simple representation of the ternary-sequence in the time-domain, it also has useful frequency-domain characteristics, as shown in Figs. 6 and 7. The even-order harmonics are suppressed in Fig. 7, which reduces the non-linear effects of the system in the measurements results [9]. Moreover, there are no sudden changes in the spectral power of the non-zero harmonics and each harmonic component is equally weighted making the measurements reliable. However, the spectral power will decrease to zero at the generating frequency $f_{\mathrm{gen}}$ of the sequence, which is 1kHz in Figs. 6 and 7. The reduction of the spectral power limits the usable bandwidth of the measurements to approximately $0.5 * f_{\mathrm{gen}}$ [5]. The sequence length $N$ along with $f_{\mathrm{gen}}$ determines the frequency resolution of the sequence given in (18), which is also the lowest frequency harmonic that is measured.

$$f_{\mathrm{res}} = \frac{f_{\mathrm{gen}}}{N}. \tag{18}$$

In terms of battery impedance measurements, the parameters in (18) play a significant role for obtaining the appropriate bandwidth for the battery impedance measurements. For the design guidelines used in this paper, the bandwidth should cover the end of the diffusion region of the battery impedance, as well as the beginning of the ohmic/inductive region. To avoid aliasing effect of the measurements, the generated ternary sequence is sampled at rate $f_{\mathrm{s}}$, which is higher than $f_{\mathrm{gen}}$. Another important parameter is the amplitude of the sequence, which is the battery current. As the battery impedance is usually very small, the current should be relatively high in order to provide an appropriate signal-to-noise ratio for

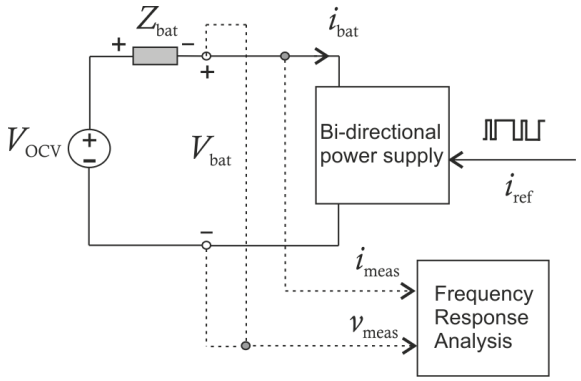


Fig. 8: Measurement setup for the battery impedance measurements

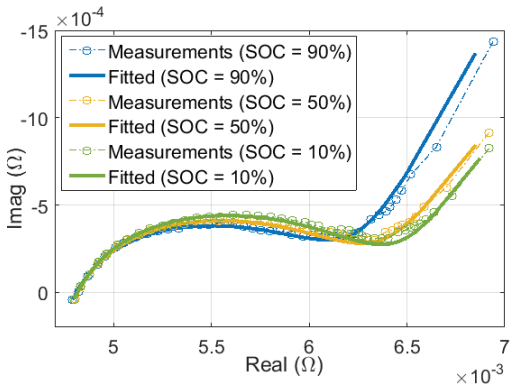


Fig. 9: Measured and fitted impedances at different SOC values

the measurements. The comprehensive characterization of the diffusion region at very low frequencies is avoided because this significantly increases the measurement time, which should be kept tolerable for online applications. The design parameters of the ternary-sequence covering the desired bandwidth, amplitude, and sampling frequency are shown in Table I. The generation algorithm of the ternary-sequence is presented in [9].

## V. Experiments

The experiment setup is illustrated in Fig. 8 where the impedance of a LiFePo4 battery cell with a nominal voltage of 3.3V and a capacity of 2.5Ah was measured. The ternary-sequence perturbation with design parameters given in Table I was injected to the battery as the current reference for the bi-directional power supply. The impedance measurements were carried out with 10 percent SOC resolution by discharging the cell to the desired SOC with a current of 1C. The current and voltage were measured and the resulting impedance spectra was filtered by moving-average-filter (MAF) to smooth the resulting spectra for the ECM fitting [11], [13]. The design of the MAF is done according to [11], where two windows with 25 percent overlap are applied to the impedance measurements due to the logarithmic nature of the impedance. The window lengths (20 for the smaller and 120 for the larger window) are chosen according to the data indices at the end of the diffusion and at the top of the semicircle of the impedance data (indices of $R_{\text{diff}}$ and $R_{\text{semicircle}}$ in Fig. 3). The temperature for the measurements was kept constant at 35°C since measurements at various temperature points were considered to be beyond the scope of this the paper.

The proposed fitting algorithm is applied to all measured impedances at 10 percent SOC intervals. The difference in (16) was selected as the convergence limit as the algorithm is stopped when the difference $R'_{\text{diffusion}} - R_{\text{diffusion}}$ is smaller than 1e-6. The maximum number of iterations was set to 30. The performance of the algorithm is analyzed in terms of root-mean-square-error (RMSE), which is defined as given in (19), where $Z_{\text{fit}}$ is the fitted impedance, $Z_{\text{meas}}$ is the measured impedance, and $N$ is the length of the impedance vectors.

$$\text{RMSE} = \sqrt{\frac{1}{N}\sum_{i=1}^{N}(1 - \frac{Z_{\text{fit}}(i)}{Z_{\text{meas}}(i)})^2} \tag{19}$$

TABLE I: Ternary-sequence design parameters for the measurements

| amplitude | $f_{\text{gen}}$ | $N$ | frequency band | $f_s$ |
|---|---|---|---|---|
| 1A | 7kHz | 32762 | 210mHz - 3.5kHz | 35kHz |

## VI. Results

The fitted impedances are showing a good match to the measured impedances in Fig. 9. The RMSE values in Table II are also showing good performance of the algorithm as the errors are less than 0.5 percent for most of the fits. The extracted parameter values for $N_{\text{D}}$, $C_{\text{D}}$, $N_{\text{CT}}$, and $C_{\text{CT}}$ in Fig. 10 can be observed to have the most linear or nearly linear variations as a function of SOC. It is widely recognized that the diffusion region is the most sensitive for the SOC variations, and $N_{\text{D}}$ and $C_{\text{D}}$ are the parameters that most dominantly characterize the low-frequency response of the impedance [2], [3]. However, the charge-transfer region parameters $N_{\text{CT}}$ and $C_{\text{CT}}$ are also showing a SOC-dependent trend along the whole SOC excluding the value at SOC=90%. The SOC dependency at the charge-transfer region parameters can be explained by the slightly increasing radius of the charge-transfer region semicircle which can be observed from Fig. 9. The error in the parameters at SOC=90% is likely to be caused by some errors in the measurement data and the distortion caused by the applied MAF. However, the algorithm is proved to work sufficiently and can provide linear or near linear dependency for the ECM parameters, which is important if the method is utilized for state-estimation in battery applications. Although the number of iterations for some cases is relatively high (30 iterations), the algorithm can be considered to be computationally light because only a few steps and calculations are required within an iteration. Moreover, the

TABLE II: Fitting errors and the number of iterations required for the algorithm to converge

| **SOC** | 10% | 20% | 30% | 40% | 50% | 60% | 70% | 80% | 90% |
|---|---|---|---|---|---|---|---|---|---|
| **RMSE** | 0.62% | 0.54% | 0.45% | 0.42% | 0.32% | 0.34% | 0.39% | 0.45% | 0.78% |
| **Iterations** | 30 | 22 | 18 | 23 | 30 | 30 | 26 | 19 | 18 |

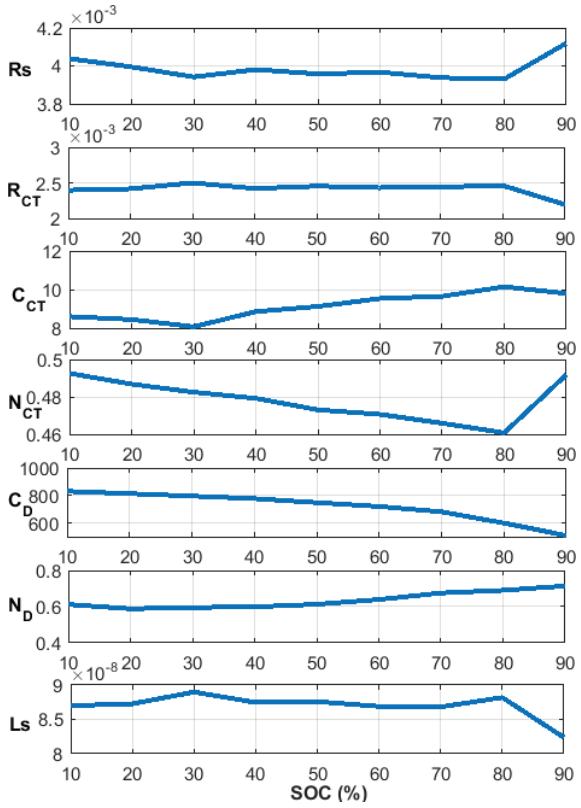


Fig. 10: Extracted ECM parameters with the proposed algorithm as a function of SOC

proposed fitting algorithm can be considered to be scalable to the SOH impedance-based estimation, even though the SOH-dependency of the parameters was not analyzed due to the long time required for the battery aging to obtain experiment data.

## VII. Conclusions

This paper has presented a novel fitting algorithm for extraction of the battery ECM parameters from the measured impedance data. The performance of the method is shown for real LiFePo4-cell impedance data measured with a three-level PRS signal. It is shown that the proposed method is computationally light to implement and provides accurate fit to the impedance data. The extracted parameter values, which are widely recognized as SOC-dependent parameters, are observed to have clear dependency to the battery SOC. Therefore, the algorithm could be used to improve the Li-ion battery state-estimation. Together with the ternary-sequence measurements, the proposed algorithm could also be utilized for online battery applications.

## References


[1] S. Vazquez, S. M. Lukic, E. Galvan, L. G. Franquelo, and J. M. Carrasco, "Energy Storage Systems for Transport and Grid Applications," *IEEE Trans. Ind. Electron.*, vol. 57, no. 12, pp. 3881–3895, 2010.

[2] P. Weicker, *A system Approach to Lithium-ion Battery management*. Artech House, 2013, no. 2013.

[3] J. Meng, M. Ricco, G. Luo, M. Swierczynski, D. Stroe, A. Stroe, and R. Teodorescu, "An overview and comparison of online implementable soc estimation methods for lithium-ion battery," *IEEE Transactions on Industry Applications*, vol. 54, no. 2, pp. 1583–1591, March 2018.

[4] M. Berecibar, I. Gandiaga, I. Villarreal, N. Omar, J. Van Mierlo, and P. Van den Bossche, "Critical review of state of health estimation methods of Li-ion batteries for real applications," *Renewable and Sustainable Energy Reviews*, vol. 56, pp. 572–587, apr 2016.

[5] K. Godfrey, *Perturbation Signals for System Identification*. Prentice Hall, 1993.

[6] W. Huang and J. A. Qahouq, "An online battery impedance measurement method using DC-DC power converter control," *IEEE Trans. Ind. Electron.*, vol. 61, no. 11, pp. 5987–5995, 2014.

[7] E. Din, C. Schaef, K. Moffat, and J. T. Stauth, "A scalable active battery management system with embedded real-time electrochemical impedance spectroscopy," *IEEE Transactions on Power Electronics*, vol. 32, no. 7, pp. 5688–5698, 2017.

[8] D. A. Howey, P. D. Mitcheson, S. Member, V. Yufit, G. J. Offer, and N. P. Brandon, "Motor Controller Excitation," *IEEE Trans. Veh. Technol*, vol. 63, no. 6, pp. 2557–2566, 2014.

[9] A. H. Tan and K. R. Godfrey, "The generation of binary and near-binary pseudorandom signals: An overview," *IEEE Transactions on Instrumentation and Measurement*, vol. 51, no. 4, pp. 583–588, 2002.

[10] J. Sihvo, T. Messo, T. Roinila, and D. I. Stroe, "Online identification of internal impedance of Li-ion battery cell using ternary-sequence injection," in *Energy Conversion Congress and Exposition (ECCE), 2018 IEEE*, 2018, pp. 1–7.

[11] J. Sihvo, D. Stroe, T. Messo, and T. Roinila, "A fast approach for battery impedance identification using pseudo random sequence (prs) signals," *IEEE Transactions on Power Electronics*, pp. 1–1, 2019.

[12] T. Roinila and T. Messo, "Online Grid-Impedance Measurement Using Ternary-Sequence Injection," *IEEE Transactions on Industry Applications*, vol. 54, no. 5, pp. 5097–5103, sep 2018.

[13] P. Manganiello, G. Petrone, M. Giannattasio, E. Monmasson, and G. Spagnuolo, "Fpga implementation of the eis technique for the online diagnosis of fuel-cell systems," in *2017 IEEE 26th International Symposium on Industrial Electronics (ISIE)*, June 2017, pp. 981–986.

[14] P. Vyroubal and T. Kazda, "Equivalent circuit model parameters extraction for lithium ion batteries using electrochemical impedance spectroscopy," *Journal of Energy Storage*, vol. 15, pp. 23–31, feb 2018.

[15] S. R. Nelatury and P. Singh, "Equivalent circuit parameters of nickel/metal hydride batteries from sparse impedance measurements," *Journal of Power Sources*, vol. 132, no. 1-2, pp. 309–314, 2004.

[16] S. M. M. Alavi, C. R. Birkl, and D. A. Howey, "Time-domain fi tting of battery electrochemical impedance models," *Journal of Power Sources*, vol. 288, pp. 345–352, 2015.

[17] D.-I. Stroe, M. Swierczynski, A.-I. Stroe, and S. Knudsen Kær, "Generalized Characterization Methodology for Performance Modelling of Lithium-Ion Batteries," *Batteries*, vol. 2, no. 4, p. 37, 2016.

[18] S. M. R. Islam and S.-y. Park, "Circuit Parameters Extraction Algorithm for a Lithium-Ion Battery Charging System Incorporated with Electrochemical Impedance Spectroscopy," *2018 IEEE Applied Power Electronics Conference and Exposition (APEC)*, pp. 3353–3358, 2018.